RSC Mechanochemistry

ROYAL SOCIETY OF CHEMISTRY

PAPER

View Article Online
View Journal | View Issue

Cite this: *RSC Mechanochem.*, 2025, **2**, 901

X-ray diffraction study of the polymorphism in Er_2O_3 driven by ball milling

Ana Maria Constantin, [a] Francesco Mele, [a] Daniele Alessandro Cauzzi,[a] Raimondo Maggi, [a] Elena Villa,[b] Alessandro Cerveri[a] and Lara Righi *[a]

Polymorphic transformations in rare-earth sesquioxides (RE-SOs) are accessible *via* ball-milling. Prolonged mechanical grinding induces the formation of denser polymorphic structures, replicating the phenomena typically observed under high-pressure conditions. In this study, Er_2O_3 cubic phase with bixbyite structure (C-type) was subjected to different milling sessions with diverse vibrational milling frequencies. X-ray diffraction experiments combined with Williamson–Hall (W–H) and Rietveld analysis were adopted to study the microstructural aspects encompassing crystal size, microstrain, and unit cell distortion. As the frequency increased, the transition from the Er_2O_3 cubic to the monoclinic denser structure (B-type) was partially activated. When the milling frequency reached the critical condition, the polymorphic transformation was completely realized. The analysis of the microstructural changes triggered by high frequency milling discloses the key-role of the microstrain, rather than the reduction of the crystal size, in driving the structural transition from cubic to monoclinic polymorphs. Furthermore, ball milling conducted at the highest frequency promotes, rather than amorphization, the formation of the polymorphic form exhibiting a fluorite (CaF_2)-type structure, indicating the presence of point lattice defects involving oxygen vacancies. As a result, the structural analysis revealed the distinct role of microstructural features in promoting polymorphism within RE-SOs.

Received 27th February 2025
Accepted 1st September 2025

DOI: 10.1039/d5mr00033e

rsc.li/RSCMechanochem

1 Introduction

Rare-earths sesquioxides (RE-SOs) are well known in materials science and chemistry for their distinctive properties, including high thermal stability, optical characteristics and catalytic activity, which enable a wide spectrum of advanced technological applications.[1,2] RE-SOs, particularly lanthanide SOs (Ln_2O_3; Ln = La to Lu, including Y and Sc), crystallize in either the A-, B-, or C-type polymorphic structures (refer to Fig. S1 for the corresponding X-ray diffraction patterns), depending on the RE atomic radius and temperature conditions.[3–6] The archetypal structure of RE-SOs (C-type), exhibits the cubic bixbyite-type of symmetry, whereas the polymorphs B and A show monoclinic and hexagonal structures, respectively.[7,8] Notably, the relative stability of the different polymorphs is also dependent on the pressure conditions.[7] When subjected to high pressure, RE-SOs experience changes in the coordination of the trivalent metal, leading to more compact structures, thereby inducing the C → B phase transition. For SOs composed of lighter metals, such as La_2O_3, this transition typically occurs at pressures in the range of 8–20 GPa.[9] Further increments of the applied pressure determine the conversion from monoclinic B polymorph to A-type, showing the most dense crystal structure.[10]

It has been widely reported[11] that irreversible polymorphic transformations in metal oxides, triggered by high-pressure compression, can also occur during ball milling under atmospheric conditions. In TiO_2 the mechanical activation is responsible for the switching from anatase to the more thermodynamically stable rutile phase. Mechanical milling induces the conversion of monoclinic zirconia (ZrO_2) into the tetragonal phase, especially when combined with yttria doping.[12] Extended milling and high-energy impacts can further stabilize the cubic phase of zirconia, which is often used in thermal barrier coatings.[13] Furthermore, polymorphic transformations resulting from high-energy milling treatments have been also observed in some RE-SOs.[14] In the case of Y_2O_3,[15,16] the extended high energy ball milling induces the formation of a mixture of monoclinic B polymorph and a partially amorphized phase.

The mechanical milling process entails severe plastic deformation and particle fragmentation. During the milling process, repeated cycles of cold welding and fracturing resulted in a broad grain size distribution.[11,17,18] Such a deviation from equilibrium induces intrinsic defects beyond the critical density, which can lead to structural rearrangements and polymorphic transformations under atmospheric conditions.[11,14] Nevertheless, the relationship between the alteration of microstructural parameters induced by mechanical grinding

[a]*Department of Chemistry, Life Science and Environmental Sustainability, University of Parma, Parco Area delle Scienze 17/a, Parma, 43124, Italy. E-mail: lara.righi@unipr.it*

[b]*CNR ICMATE, Unit of Lecco, Via G. Previati 1/E, 23900, Lecco, Italy*

and polymorphic transitions in RE-SOs has not yet been fully elucidated.[19]

In this study, the polymorphic structural transitions of Er_2O_3 occurring under mechano-treatment at room temperature were investigated. The cubic C-type phase of Er_2O_3 was subjected to different milling conditions and the resulting crystalline phases were studied by X-ray diffraction. The structural analysis was focused on the variation of the microstructural aspects related to the crystal size, micro-strain and uniform lattice strain in response to the applied mechanical grinding. These findings reveal that each microstructural feature plays a distinct role in determining the observed C → B structural change. The thermal stability of the Er_2O_3 B-polymorph stabilized at room temperature was investigated and the temperature of the reverse B → C change was determined. The effects of ball milling on the structural evolution of RE-SOs provide insights for the rational mechanochemical production of nanocrystalline phases with desired physical properties.

2 Experimental details

Pulverisette 23 Mini-Mill from FRITSCH was employed for all ball milling operations on Er_2O_3 powder (99.99% purity) obtained from Sigma-Aldrich. Each milling session involved grinding 200 mg of the Er_2O_3 C-phase in a 15 ml zirconia container using a pair of 15 mm diameter zirconia balls with a ball-to-powder ratio (BPR) of 60 : 1. The Er_2O_3 specimens were milled at various frequencies ranging from 15 to 45 Hz for durations ranging from 1 to 6 hours (h). Each milling session utilized a new sample to avoid the repeated processing of the same powder.

Powder X-ray diffraction (PXRD) data were obtained from Er_2O_3 milled samples using a Rigaku Smartlab Multipurpose diffractometer with a HyPix3000 two-dimensional detector (Rigaku, Tokyo, Japan). The diffraction patterns were collected at room temperature using Bragg–Brentano geometry with CuKα radiation and a 2θ angular range extending from 15° to 65°, with a scan rate of 5° min^{-1} and a step size of 0.02°. The determination of crystal size and microstrain featuring the samples obtained for milling frequencies ranging between 15 and 25 Hz (except for the sample corresponding to 25 Hz-6 h conditions) was obtained by adopting the Williamson–Hall (W–H) method.[20] Rietveld refinements and/or profile fitting of Er_2O_3 were carried out by using the Jana2020 software package.[21]

Er_2O_3 samples before and after milling sessions were analyzed using an Environmental Scanning Electron Microscope (ESEM) Quanta™ 250 FEG (FEI, Hillsboro, OR, USA). The accelerating voltage was 10 kV and the secondary electron signal was collected by a gaseous secondary electron detector (GSED) to generate micrographs for morphological studies. Potential contamination from the milling media was assessed using Energy-Dispersive X-ray Spectroscopy (EDX).

FT-IR spectrometry was carried out on starting and milled samples of Er_2O_3 with a PerkinElmer FT-IR spectrometer. The absorption spectra are presented in the SI.

Differential Scanning Calorimetric (DSC) was performed using a DSC25 TA Instruments Calorimeter equipped with Finned Air Cooling System (FACS). The investigation of reversing and non-reversing contributions to total heat flow was carried out under modulated temperature ramp condition (MDSC), with rate of 2 °C min^{-1}, $\Delta T = \pm 0.5$ °C on period time of 90 s.

3 Results and discussion

Er_2O_3 exhibits a cubic bixbyite-like crystal structure with space group $I\bar{3}a$ having $Z = 16$. PXRD analysis (see Fig. S2) indicated a unit cell parameter of $a = 10.537(8)$ Å with the volume normalized on multiplicity site V/Z of 73.11 Å^3, in agreement with the expected values for the Er_2O_3 ground state.[22] The microstructural parameters of the starting Er_2O_3 compound were determined by applying the Williamson–Hall (W–H) method[23] to split crystal size and microstrain contributions from the integral breadth of the diffraction peaks. The instrumental contribution to the peak shape was determined through the analysis of the diffraction pattern of the standard Al_2O_3 and modelled with Caglioti parameters.[24] Considering the good crystallinity of the starting material, we selected the region 30–80° of 2θ for peak fitting and efficiently separating the Kα1 and Kα2 diffraction lines. The linear regression of the W–H diagram, reported in Fig. S3, defines the Scherrer crystal size and the microstrain of the starting material. To validate the results obtained by the W–H method, Rietveld fitting was performed with JANA2020 software.[21] The best fitting, as demonstrated in Fig. S2, exhibits agreement factors of $R_p = 4.24\%$ and $R_{wp} = 5.26\%$. This structural refinement was achieved by incorporating both the Lorentzian LX and LY parameters of the pseudo-Voigt function, which correspond to the contributions of crystal size and microstrain, respectively.[24]

According to the W–H analysis, consistent with the Rietveld fitting, the starting material was formed by crystalline domains having an average size of 100(5) nm and was essentially unaffected by structural strain. (Fig. 1a) depicts the SEM micrograph, indicating that Er_2O_3 is composed of plate-like aggregates of microcrystals. The anisotropic crystal shape was also manifested by the preferred orientation observed in the powder diffraction data (see Fig. 1b). For instance, the optimal profile fitting was obtained by including a preferred orientation correction for $h0h$ with $h = 2n$ reflections, accompanied by a reduced intensity of the $h00$ reflections (Fig. 1c). exhibits the crystal habit consistent with the indications from PXRD and SEM measurements.

Er_2O_3 was subjected to milling sessions where duration and frequency were systematically modified while keeping BPR unvaried. Distinct vibrational frequencies ranging from 15 to 45 Hz were selected, with a maximal milling duration of 6 h. Fig. 2 shows the diffraction patterns of the Er_2O_3 powders after milling sessions of 6 h with incremental vibration frequency. In general, for low-energy conditions, between 15 and 20 Hz, no polymorphic transition was observed (as indicated in Fig. S4), whereas progressive conversion from C to B polymorphs was observed for frequencies exceeding 20 Hz.

For milling performed at 20 Hz, Er_2O_3 exhibited a progressive decrease in crystal size combined with incremental

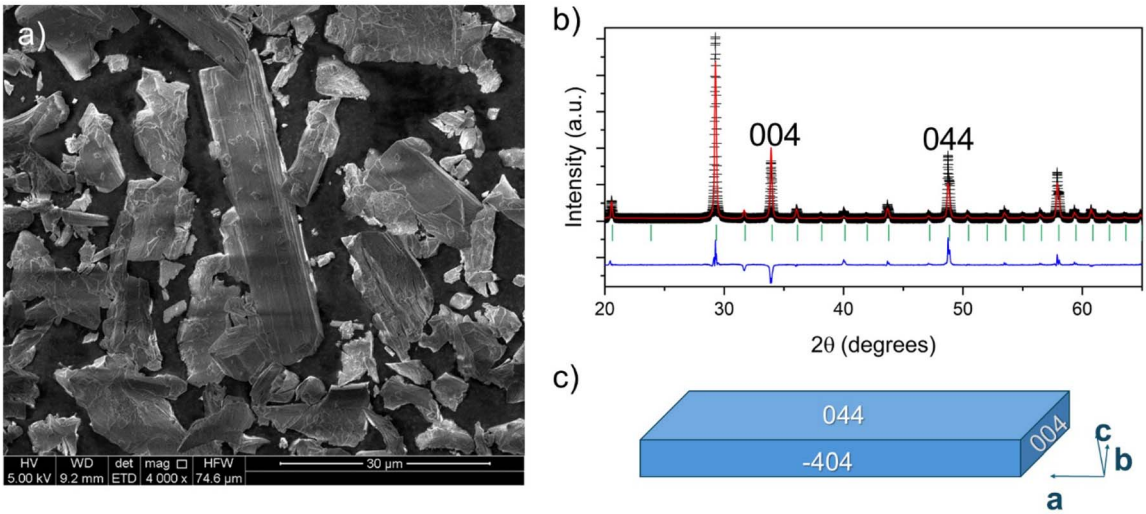

Fig. 1 (a) SEM micrograph showing the elongated platelet-like shape of Er_2O_3 crystals prior to milling. (b) Direct comparison of the calculated (red line) and experimental (black symbols) diffraction patterns. The preferred orientation of the microcrystals is evidenced by the observed intensity of the 044 reflection. (c) Proposed crystal habit indicating the extension of the 0*hh* faces, in agreement with SEM and XRD measurements.

microstrain. Fig. 3 depicts the respective values of microstrain and crystal size extrapolated by W–H approach applied to the corresponding diffraction patterns (see Fig. S2b–d). Both structural characteristics depend linearly on the milling hours (MH) but their evolution with the increment of frequency is basically different. The crystal size gradually decreased, but the mean values, as shown in (Fig. 3a), did not exhibit significant variations with increasing milling energy. In contrast, the microstrain exhibited greater sensitivity to the frequency of the milling process. As illustrated in (Fig. 3b), the structural strain progressively increased with the milling duration; however, this increase was significantly more pronounced at higher frequencies.

The diffuse scattering between 30–34 degrees of 2θ, featuring the 25 Hz-3 h sample (Fig. S4), suggests the initial formation of a nanocrystalline monoclinic B-Er_2O_3 phase. The 2θ region of diffuse scattering corresponding to the most intense reflections of the monoclinic polymorph indicates that the structural switching is more energetically favorable, under low energy milling conditions, rather than the amorphization of the cubic phase. This interpretation is corroborated by the observed increase in the fraction of the Er_2O_3 monoclinic variant in the 25 Hz-6 h combination, coexisting with highly strained cubic C-type phase.

The presence of two nanocrystalline phases prevents the application of the W–H approach. To estimate the fraction of the two polymorphs in the sample corresponding to 25 Hz-6 h, a Rietveld refinement was performed. The existence of amorphized material was checked by adopting the direct Rietveld method[25,26] and successfully applied in the determination of amorphous content in glass-ceramics and composite materials.[27,28] This method allows the extrapolation of the

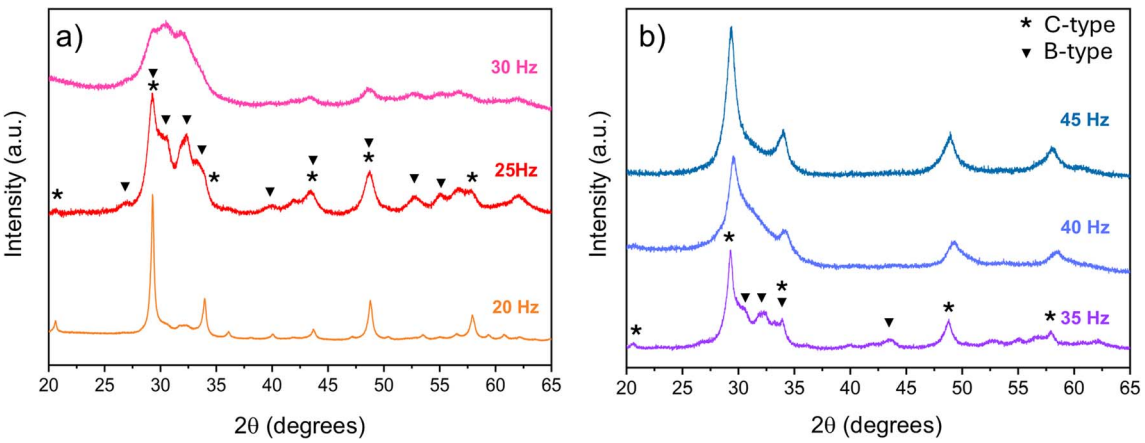

Fig. 2 (a) PXRD for Er_2O_3 milled at frequencies from 20 to 30 Hz for 6 h. (b) PXRD for Er_2O_3 milled at frequencies ranging from 35 Hz to 45 Hz for 6 h.

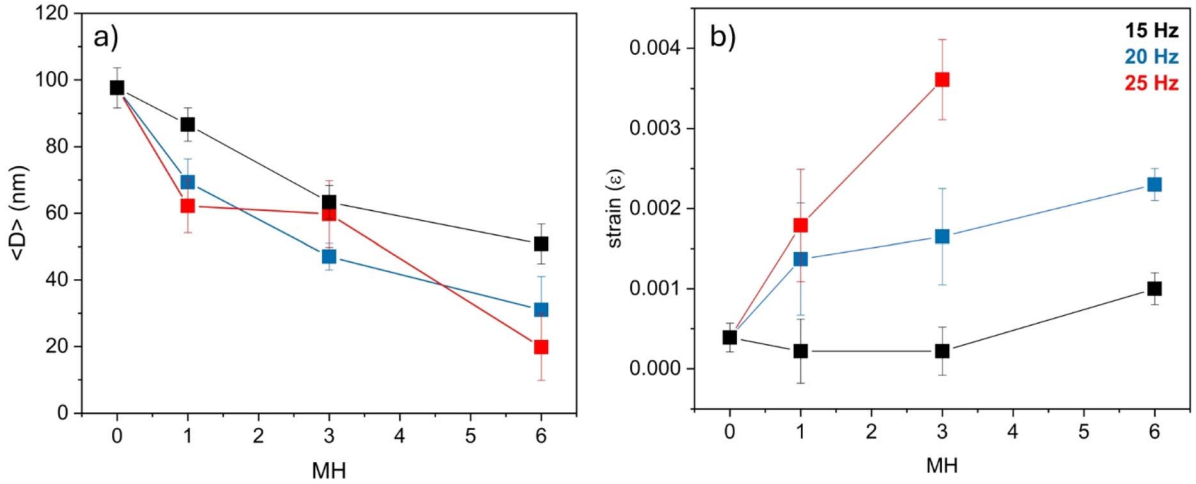

Fig. 3 Variation of crystal size (a) and microstrain (b) calculated using the W–H approach for Er_2O_3 C-type phase ball milled at 15 Hz, 20 Hz, and 25 Hz over milling hours (MH). The crystal size reported for the sample treated at 25 Hz-6 h was determined by quantitative Rietveld analysis. The microstrain parameter was not refined during the Rietveld analysis due to the presence of the B-type polymorph (further details are provided in the Section 3.1 of SI). The straight lines serve as visual guides.

approximate relative amount of the crystalline and amorphous phases without the incorporation of internal standards in the powders prepared for diffraction measurements.[26] Further details are illustrated in the Section 3.1 of SI. When milling was performed at 25 Hz for 6 h, Rietveld analysis (Fig. S5) did not reveal a significant presence of an amorphous phase. The relative quantities of the two polymorphs, detailed in Table S1, show partial conversion from C to B.

The non-uniform structural strain of the cubic phase, responsible for the peak broadening, is accompanied by a uniform lattice strain manifested by the progressive increase of the unit cell parameter *a*. The volume change of C-Er_2O_3 for increasing milling frequencies is shown in Fig. 4a. As the milling energy is augmented, the unit cell volume change $\Delta V/V$ displays a progressive increase indicating the dilatation of the interplanar distances of the crystal structure. It has been recurrently observed that several nanocrystalline inorganic oxides,[29–37] such as TiO_2, ZrO_2 and CeO_2, which are not necessarily obtained by ball milling, are characterized by the gradual expansion of the unit cell parameters as the crystal size progressively decreases. Md. Imteyaz Ahmad and co-workers[34] attributed the enlargement of unit cell parameter of TiO_2 nanocrystals as originated by the weakening of several superficial bonds, causing the formation of oxygen vacancies and subsequent expansion of the surface.

Fig. 4b shows that the unit cell parameter of milled C-type Er_2O_3 linearly increases with the diminution of crystal size, in agreement with TiO_2-anatase behaviour.[34] By adapting the empirical relation proposed by Md. Imteyaz Ahmad,[34] the unit cell change against crystal size can be written as:

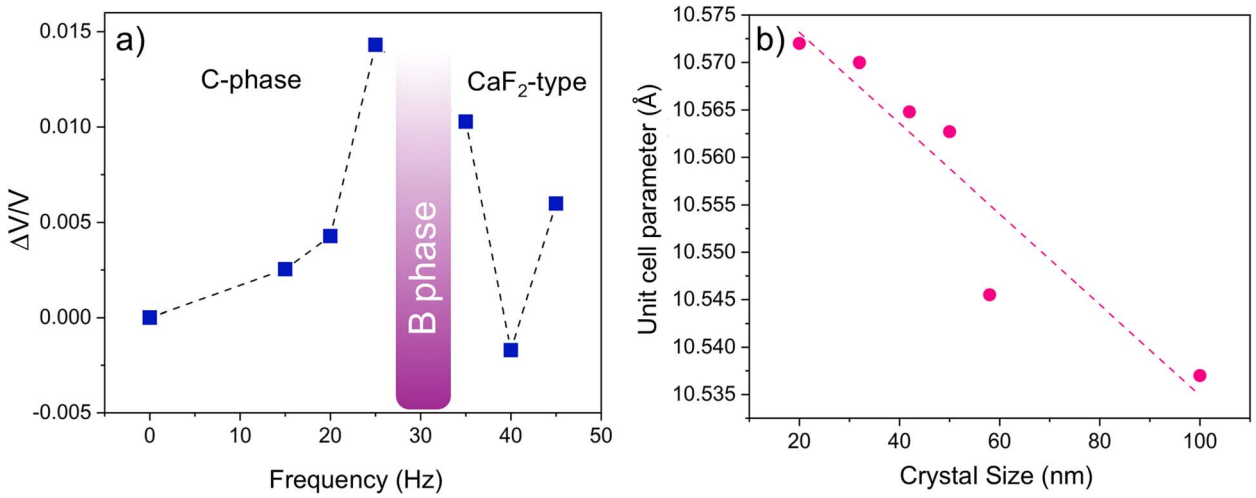

Fig. 4 (a) Volume changes ($\Delta V/V$) for the C-polymorph and fluorite-type phase (using 2 × $V_{fluorite}$ for direct comparison) across all milling frequencies (15–45 Hz) after 6 hours processing. The unit cell parameters were determined by Rietveld refinements. (b) Dependence of the unit cell parameter on the crystal size for the C-polymorph determined by W–H method. The dotted line represents the linear regression.

$$a = a_0 + \frac{A}{D} \quad (1)$$

where A is constant, and D is the crystals size expressed in nanometers.

The linear fitting (see Fig. S6) of the unit cell values *versus* $1/D$ returns a unit cell parameter $a_0 = 10.5377$ Å for well crystallized grains. The strong agreement between the extrapolated unit cell parameter and the refined value for pristine C-type Er_2O_3 suggests that the observed lattice expansion could be originated from surface stress effects in the milled nanoparticles.[38] This phenomenon is analogous to observations in CeO_2 nanocrystals, where size-dependent lattice expansion has been ascribed to the formation of oxygen vacancies and the incorporation of Ce^{3+} ions.[39] While adsorbed species (CO_2, H_2O) can contribute to such expansion in related nanocrystalline systems,[36] IR spectroscopy of the milled Er_2O_3 (Fig. S7) showed no detectable surface adsorbates, ruling out this mechanism. Therefore, for nanocrystalline Er_2O_3 particles (20–100 nm), the description of the primary mechanism responsible for lattice expansion requires further investigations. However, the existing evidence suggests that the formation of surface-mediated point defects is the most plausible explanation.[38]

The 30 Hz-6 h sample showed the characteristic diffraction pattern of the Er_2O_3 monoclinic phase (B-polymorph). Therefore, the C → B conversion was complete with the concomitant limited formation of amorphous material (see Table S2). The broadening of the diffraction peaks prevents precise determination of the unit cell constants. Nevertheless, the cell parameters of the monoclinic crystal structure with space group $C2/m$ provided by the fitting shown in Fig. S8 and summarized in Table 1, are consistent with the B-polymorph quenched under ambient conditions after the application of 16 GPa.[40] Thus, after 6 h of milling at 30 Hz, the system underwent a transformation into the denser B-polymorph, showing the lower V/Z ratio with an average crystal size of 12(5) nm. SEM analysis, evidenced in Fig. S9a, reveals that Er_2O_3 B-type particles exhibit smooth edges and a flake-like morphology, suggesting the occurrence of extended plastic deformation. Furthermore, as depicted in Fig. S9b, energy-dispersive X-ray (EDX) spectroscopy revealed the presence of marginal zirconium contamination originating from the balls and the container utilized during the milling sessions.

The transition from the cubic to monoclinic phase under high pressure resulted in a 9% decrease of the initial volume.[7,40] In the milling-induced structural change, the irreversible volume contraction of 9.2% is in good agreement with earlier studies, indicating that the milling conditions provide a virtual compression comparable to the high-pressure regime. Evidence of irreversible transformation to polymorphic forms stabilized at high pressure during mechano-treatment in inorganic materials is well established in the literature.[11,14] Prolonged ball milling sessions on anatase TiO_2 yielded a partial transformation from the tetragonal phase to the denser cubic phase.[41] In the context of the RE-SOs, the C → B transition induced with high energy milling has been documented for Y_2O_3.[11,15,16] Vaishnavi Krupa *et al.*,[16] reported that the complete transformation of yttria, after 30 h of milling, is achieved when the crystal size reaches the critical value of ~12 nm, in accordance with the observed dimensions of the particles of Er_2O_3 B-polymorph.

The direct transformation from C to B-type structure in M_2O_3 has also been obtained through the application of a mechanical shock.[42,43] Specimens, comprising Eu_2O_3, were subjected to shock loading reaching 2–50 GPa[42] using flyer plates accelerated by a propellant gun. During instantaneous compression, the system undergoes structural changes, indicating a fast and multi-step conversion. The phase transition from the C-to the B-type structure was proposed to proceed *via* the hexagonal A-type structure. The shock induced transformation results in the fast transformation C → A followed by the fast conversion A → B during pressure release. The structure of the A-phase is similar to that of the B-type and the rearrangement of some anion positions occurring during the transition can account for the observed rapid kinetics. Furthermore, a recent experiment[44] showed that a single ball impact, realized by dropping a tungsten carbide (WC) sphere, can initiate solid-state transformations. Nevertheless, the structural evolution in Er_2O_3 depending on the energy imparted during milling cannot be ascribed exclusively to the instantaneous compression occurring during multiple impacts. In analogy with earlier studies,[11,14,45] the progressive microstructural modifications introduced by dynamic shear play a fundamental role in defining the relative stability of polymorphic forms in Er_2O_3.

In this scenario, the crystal size and microstrain can be considered from different perspectives. It has been recurrently observed that if the starting material is formed by nanosized crystals, the polymorphic transformations induced by pressure application shift towards higher pressure regimes.[46,47] When C-phase Er_2O_3 subjected to high pressure is formed by nanocrystals below 20 nm, the onset of the phase transition shifts from 9.9 GPa to 17 GPa.[47] Moreover, analogously to what is observed in shock-induced transitions, the sequence of polymorphs stabilized under pressure is altered being C → A instead of C → B. Such behaviour highlights the size-dependence of the bulk modulus, which is higher for nano-

Table 1 Structural data for the cubic Er_2O_3 (C-type) starting material and monoclinic Er_2O_3 (B-type) phase obtained at 30 Hz for 6 hours

Phase label	Unit cell parameters (Å, degrees)	V (Å^3)	Symmetry	Z	Density (g cm^{-3})	V/Z
C-Er_2O_3	$a = 10.5376(4)$	1169.83(4)	$I\bar{3}a$	16	8.69	73.11
B-Er_2O_3	$a = 13.91(7)$, $b = 3.4(3)$, $c = 8.6(1)$, $\beta = 100.2(9)°$	407.00(21)	$C2/m$	6	9.36	67.83

Er_2O_3 if compared to the corresponding crystalline isostructural material.[47] Similar size effects in driving the phase transformations have been observed in other oxides.[48,49] Therefore, earlier literature suggests that the progressive decrease of the crystal dimensions induced by milling would imply the shift of the critical pressure required to trigger the structural conversion. The ongoing concomitant alteration of microstructural characteristics, mainly related to the structural nonuniform strain, does not allow a simple correlation between the crystal size and instantaneous pressure generated during ball impacts. For instance, the trends shown in Fig. 3a and b suggest that the leading parameter ruling the C → B transition is represented by the structural strain rather than the reduction in the crystal size. When Er_2O_3 was exposed to 25 Hz-6 h, the microstrain reached the critical threshold required to trigger the polymorphic conversion, as it is evidenced by the XRD pattern showing a relevant portion of the B-phase.

The B-type Er_2O_3 is thermodynamically unstable at atmospheric pressure and below 2000 °C.[7] The irreversible nature of the transformation induced by pressure can be attributed to the high kinetic barrier related to crystal reconstruction.

The phase transformation from the monoclinic phase back to the low-pressure phase can be realized by performing heat treatment on the ball milled phase. Fig. 5 illustrates the MDSC analysis performed on the B-Er_2O_3 phase obtained under 30 Hz-6 h. A broad, exothermic, non-reversible event was observed at 576 °C. The lack of a narrow peak corresponding to the B → C conversion suggests that the structural reconversion assumes a sluggish character with possible analogy to a reconstructive transition. The transition enthalpy $\Delta H = 5.25$ kJ mol^{-1} (see Fig. S10), albeit underestimated due to the presence of amorphous, is consistent with values[7,50] reported in calorimetric studies focused on C → B transition in other RE-SOs. Fig. 5b, showing the diffraction pattern of nanocrystals of B-Er_2O_3 milled at 30 Hz-6 h after annealing carried out at 600 °C for 1 h, indicates the complete restoration of the C-polymorph.

As shown in Fig. 2, Er_2O_3 treated at 35 Hz for 6 h was composed of nanocrystals of the B and C phases. The fitting of the diffraction pattern was performed with Rietveld method by modelling the peak broadening by the sole crystal size parameter for both phases (see Fig. S11). Quantitative analysis of the amorphous phase was attempted by incorporating a third phase having a crystal size smaller than the unit cell parameters of the monoclinic phase.[25,26] The reciprocal amounts of the Er_2O_3 phases composing the sample treated at 35 Hz-6 h are summarized in Table S3 of the SI. To validate the assessment of the amorphous content as extrapolated by direct Rietveld refinement, a second diffraction experiment, shown in Fig. S12, was carried out by incorporating Al_2O_3 as internal standard.[26,51] The amorphous content, extrapolated with the procedure illustrated in the Section 3.2 of SI and summarized in Table S4 shows a good agreement, within experimental uncertainty, with the fraction obtained with the Rietveld-based method. When the frequency exceeds 35 Hz, the amorphization becomes competitive with respect to the C → B transition observed at 30 Hz. The diffraction pattern corresponding to Er_2O_3 milled at 40 Hz-6 h reveals a relevant amount of amorphous, with the presence of highly distorted cubic phase at the nanoscale. This phase exhibits a notable contraction of the unit cell volume, as illustrated in Fig. 3a. The diffuse scattering of the amorphous material corresponds to the most intense peaks of the B-polymorph, as evidenced by the diffraction pattern of the sample 40 Hz-3 h shown in Fig. 6. Therefore, the amorphization process appears to involve the B polymorph rather than the C-type, indicating that such different behaviour could be related to the different bulk moduli characterizing the two polymorphs.[52,53]

Rietveld analysis, as depicted in Fig. S13 and reported in Table S5, indicated that Er_2O_3 ground at 40 Hz for 6 hours consists of approximately 45% cubic phase and 55% amorphous content. Nevertheless, the quantitative analysis employing the internal standard (see Fig. S14 and Table S6), revealed a reduced amount of the non-crystalline phase, suggesting a potential overestimation in the direct Rietveld refinement. As discussed in ref. 26 and detailed in the Section 4.2.1 of SI, when the intensity contributions from amorphous phases are

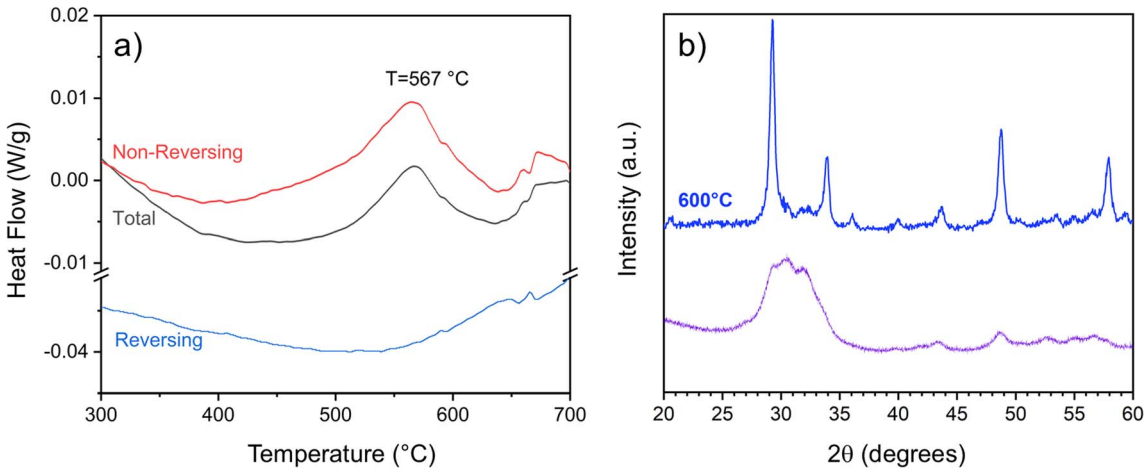

Fig. 5 (a) MDSC analysis performed on the B-Er_2O_3 phase stabilized at 30 Hz for 6 h (exothermic event is shown upward). (b) PXRD measurements before and after annealing at 600 °C for 1 h.

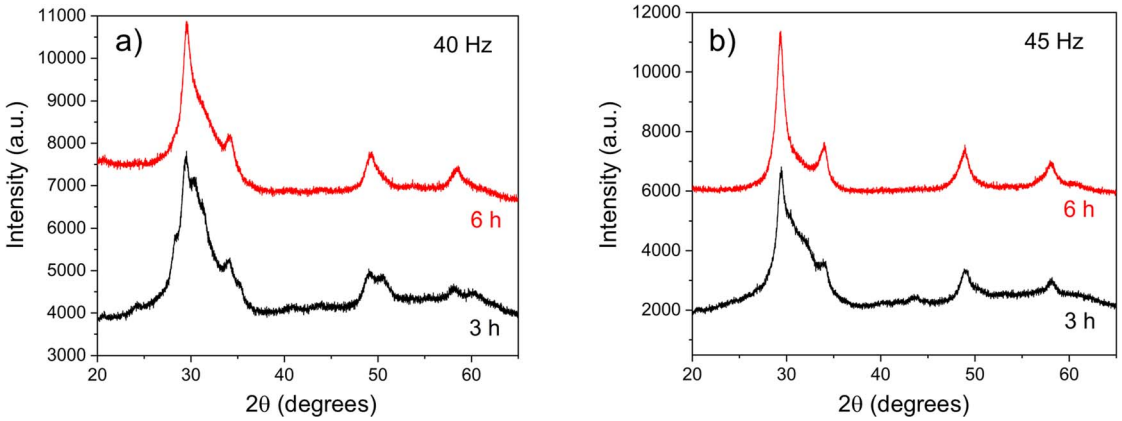

Fig. 6 (a) PXRD data for Er_2O_3 subjected to 40 Hz for 3 and 6 h. (b) PXRD data for Er_2O_3 subjected to 45 Hz for 3 and 6 h.

apparent, methods that directly model the amorphous component offer greater accuracy compared to indirect approaches. The observed discrepancies emphasize the difficulty of quantitatively analysing the partially amorphized mechanochemical products.

When the milling frequency was adjusted to 45 Hz, a comparable composition can be obtained within 3 h. The PXRD pattern of Er_2O_3 subjected to milling frequency 45 Hz-6 h, shown in Fig. 7, shows the suppression of reflections related to the bixbyite superstructure, thus suggesting the formation of highly defective fluorite-type cubic phase. Contrary to expectations, the diffuse scattering observed for Er_2O_3 milled at 40 Hz-6 h was significantly reduced. The profile fitting depicted in Fig. S15 indicates that the nanocrystalline phase shows an average crystal size = 6(4) nm and exhibits $a_{fluorite} \approx a_C/2 =$ 5.2709(5) Å, in agreement with the absence of superstructure reflections typical of the I-centered cubic phase. Furthermore, as shown in Fig. 7, the peak shapes of the 111 (28° of 2theta) and 200 (33° of 2θ) reflections and the diffuse scattering in between them likely indicate the presence of stacking faults. The fluorite-type disordered phase was observed in the RE-SOs after the application of ion irradiation. M. Tang. and co-authors[54] analysed the effects of ion irradiation on the crystal structure of RE-SOs comprising Dy_2O_3, Er_2O_3, and Lu_2O_3. Grazing incidence X-ray diffraction (GIXRD) experiments[54] indicated that the irradiation of ions at high energy induced order to disorder transformation with a change from ordered bixbyite cubic structure (C-polymorph) to a disordered, anion-deficient fluorite structure. The fluorite (CaF_2) structure displays a F-centred lattice. The structural conversion, schematized in Fig. 8, is primarily driven by the formation of extended oxygen vacancies, which induce the reorganization of the Er^{3+} coordination environment. The ~6% expansion in the Er–Er interatomic distances reflects the lattice relaxation accompanying this transition induced by high-energy milling.

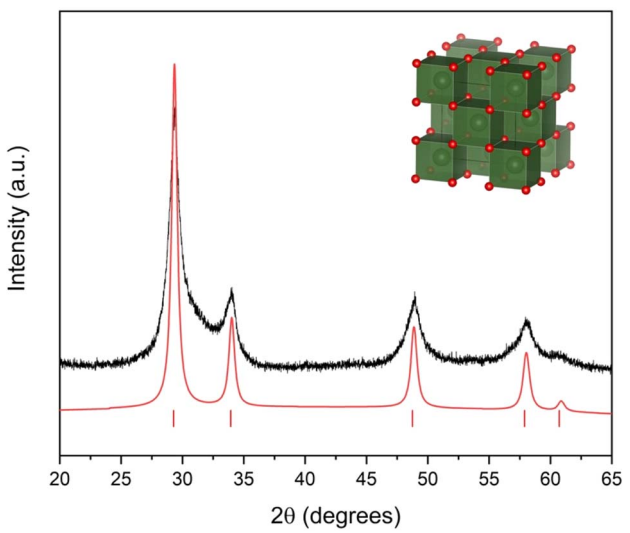

Fig. 7 Experimental (black) X-ray diffraction profile for the 45 Hz-6 h sample, compared to the calculated one (red) based on the fluorite-type structure.

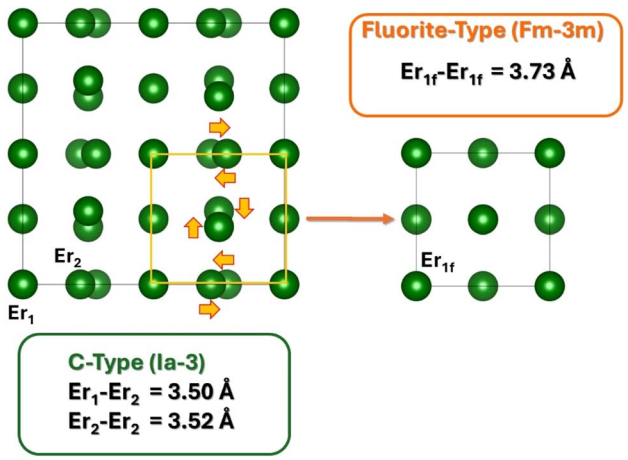

Fig. 8 Rational prospect of the structural changes of C-Er_2O_3 taking place during high frequency ball milling. The oxygen positions are neglected for clarity, whereas the green spheres represent the Er^{3+} crystal sites. The orange arrows define the atomic rearrangement of Er^{3+} occurring during the structural conversion into fluorite-type. The average Er–Er interatomic distances are reported for both phases, as determined by structural refinements.

Conversely, the decrease of the $\Delta V/V$ in the nanocrystalline cubic phase observed in the range 40–45 Hz (see Fig. 4a) is seemingly in contrast with this interpretation. In principle, the generation of oxygen vacancies governing the formation of fluorite-type phase should be accompanied by significant uniform lattice strain. On the other hand, the accommodation of the Er^{3+} cations in disordered fluorite lattice could induce relaxation of the uniform structural strain. In Bi_2O_3–Er_2O_3 solid solutions exhibiting a fluorite-like cubic structure, the unit cell parameter shows high variability depending on the oxygen ordering-disordering.[55,56] Therefore, the observed contraction of the $\Delta V/V$ should be correlated to the effective concentration of point defects associated with the lattice vacancies. The SEM micrograph in Fig. S16a reveals significant plastic deformation in the 45 Hz-6 h sample. However, this morphological examination failed to provide valuable insight into the observed contraction of the unit cell.

The structural disorder induced by the milling process at 45 Hz likely produces effects analogous to those caused by ion irradiation. This similarity was previously postulated in ref. 14. However, the phase conversion is not confined to the surface but occurs throughout the bulk volume. It may also be argued that the origin of the fluorite-type phase can be ascribed to the incorporation of Zr^{4+} ions from the jars. While minimal zirconium contamination from the milling media was detected in samples processed at 30 Hz, energy-dispersive X-ray spectroscopy (EDX) revealed significant Zr incorporation when the milling frequency exceeded 40 Hz (Fig. S16b). In $Y_2Ti_2O_7$,[57] the substitution of Zr^{4+} for the smaller Ti^{4+} ions induces the transition from pyrochlore to fluorite, primarily due to effects of cation size. However, for Er_2O_3, the incorporation of tetravalent Zr^{4+} into a trivalent cation lattice requires complex charge compensation promoting localized defect clustering and creating electrostatic barriers to long-range fluorite domain formation. This fundamental distinction suggests that while Zr contamination could likely contribute to the observed phase stability, the mechanochemical energy input remains the primary driver of structural reorganization.

The dynamic alteration of the microstructural features in Er_2O_3, triggered under mechanical action, such as structural strain, crystal size and intrinsic defects, modifies the energy landscape of polymorph stability. High pressure experiments performed on nanosized sesquioxides[46–48] indicate that the shrinking of the crystal size during milling implies the shift towards higher compression pressures for the polymorphic C → B transformation. The primary mechanical impulse driving the structural transformation towards denser B polymorph, rather than the instantaneous pressure increment, is represented by the intense torsional forces inducing structural strain, lattice defects and amorphization. Experimental works aimed at studying solid state transformation induced by rotational Bridgman devices have reported the achievement of the phase conversion under lower pressure conditions by a factor of 2 to 10.[58] Plastic deformation significantly reduces the pressure required for the initiation and completion of phase transformations in materials such as Si, Ge, and diamond-cubic structures.[59] The key factor in the substantial pressure reduction for certain phase transitions is determined by the density and type of structural defects. F. Delogu[60] emphasized the close analogy between ball milling and high-pressure torsion in determining the plastic deformation of crystals and formation of extended dislocations. In this comparative study, F. Delogu suggested the formulation of experiments conducted under torsional high-pressure conditions to disclose hidden aspects of ball milling that are not expressed in most theoretical studies. This approach can elucidate the relationship between intrinsic defects, structural strain, and polymorphic transformations in RE-SOs.

4 Conclusions

Grinding-induced polymorphism in metal oxides as well as its impact on crystal size and microstrain, are well known. To explore the influence the mechanical action in driving the polymorphic transformations, the cubic C-type phase of Er_2O_3 has been subjected to relatively short ball milling sessions. The focus was oriented on the milling frequency and its effect on crystal size, uniform ($\Delta V/V$), and non-uniform strain, as determined by structural analysis of XRD patterns. The results indicated that the complete irreversible conversion C → B involving the contraction of the molar volume typically observed under isostatic compression is primarily driven by the attainment of the microstrain threshold, which coincides with 30 Hz frequency in a vertical vibrational milling system. The nanocrystalline monoclinic B polymorph showed unit cell parameters comparable with the phase formed under high pressure.[36] When the frequency is further increased, the formation of extended oxygen vacancies induces the growth of the fluorite-like cubic phase rather than the complete amorphization. The switch to different polymorphic forms of Er_2O_3 revealed a hierarchical sequence of inherent and external structural characteristics depending on the magnitude of shear forces applied during the milling process. These findings provide valuable insights in the context of the novel emerging topic involving the fabrication of high-entropy oxides based on the stabilization of complex solid solutions assimilating multiple cations in the same crystallographic site.[61,62] In this scenario, ball milling represents an effective and sustainable method of synthesis[63,64] when polymorphism of the phases involved in high-entropy oxides is carefully evaluated.

Conflicts of interest

There are no conflicts to declare.

Data availability

The data supporting this article have been included in the SI.

Supplementary information: The Rietveld plots and associated structural data for the Er_2O_3 samples subjected to ball milling are provided in the supplementary information file. The supplementary information also includes a comprehensive description of the strategies employed for evaluating the amorphous content. Additionally, SEM micrographs, IR spectra,

and details of the thermal analysis are presented for selected Er_2O_3 samples. See DOI: https://doi.org/10.1039/d5mr00033e.

Acknowledgements

This work has benefited from the equipment and framework of the COMP-HUB and COMP-R Initiatives, funded by the 'Departments of Excellence' program of the Italian Ministry for University and Research (MIUR, 2018–2022 and MUR, 2023–2027).

References

1 A. S. Patil, A. V. Patil, C. G. Dighavkar, V. A. Adole and U. J. Tupe, *Chem. Phys. Lett.*, 2022, **796**, 39555.
2 M. Khalid Hossain, S. Hossain, M. Hafez Ahmed, M. I. Khan, N. Haque and G. A. Raihan, *ACS Appl. Electron. Mater.*, 2021, **3**, 3715–3746.
3 P. P. Fedorov, M. V. Nazarkin and R. M. Zakalyukin, *Crystallogr. Rep.*, 2002, **47**, 281–286.
4 M. Tang, P. Lu, J. A. Valdez and K. E. J. Sickafus, *J. Appl. Phys.*, 2006, **99**, 1–7.
5 N. Dilawar, D. Varandani, V. P. Pandey, M. Kumar, S. M. Shivaprasad, P. K. Sharma and A. K. J. Bandyopadhyay, *Nanosci. Nanotechnol.*, 2006, **6**, 105–113.
6 N. Sharma, J. Singh, A. Vijay, K. Samanta, S. Dogra and A. Bandyopadhyay, *J. Phys. Chem. C*, 2016, **120**, 11679–11689.
7 F. J. Manjón, J. A. Sans, J. Ibáñez and A. L. Pereira, *Crystals*, 2019, **9**, 630.
8 M. Zinkevich, *Prog. Mater. Sci.*, 2007, **52**, 597–647.
9 K. A. Irshad, N. V. Chandra Shekar and K. Sridhar, *Acta Crystallogr., Sect. A: Found. Adv.*, 2017, **73**, C1256.
10 C. Suryanarayana, *Prog. Mater. Sci.*, 2001, **46**, 1–184.
11 S. Begin-Colin, G. Le Caer, M. Zandona, E. Bouzy and B. Malaman, *J. Alloys Compd.*, 1995, **227**, 157.
12 Y. Wang and B. S. Clausen, *J. Phys. Chem. B*, 2004, **108**, 1714–1719.
13 M. Zakeri, M. Razavi, M. R. Rahimipour and B. Jamal Abbasi, *Phys. B*, 2014, **444**, 49–53.
14 G. Šepelák, V. Bégin-Colin and S. Le Caër, *Dalton Trans.*, 2012, **41**, 11927–11948.
15 M. K. Lee, E. K. Park, J. J. Park and C. K. Rhee, *J. Solid State Chem.*, 2013, **201**, 56–62.
16 B. R. Vaishnavi Krupa, A. Dasgupta, C. Ghosh and S. Kanta Sinha, *J. Alloys Compd.*, 2022, **900**, 163550.
17 P. Baláž, M. Achimovičová, M. Baláž, P. Billik, Z. Cherkezova-Zheleva, J. M. Criado, F. Delogu, E. Dutková, E. G. Gaffet, J. Francisco, R. K. I. Mitov, T. Rojac, *et al.*, *Chem. Soc. Rev.*, 2013, **42**, 7571–7637.
18 M. Broseghini, M. D'Incau, L. Gelisio, N. M. Pugno and P. Scardi, *Mater. Des.*, 2016, **110**, 365–374.
19 L. L. D. Driscoll, H. Elizabeth, B. Dong, N. Sayed Farheen, N. Wilson Jacob, C. A. O'Keefe, A. Christopher, D. J. Gardner, C. P. Grey, P. K. Allan, A. A. L. Michalchuk and P. R. Slater, *Energy Environ. Sci.*, 2023, **16**, 5196–5209.
20 A. Khorsand Zak, W. H. Abd Majid, M. E. Abrishami and R. Yousefi, *Solid State Sci.*, 2011, **13**, 251–256.
21 V. Petříček, L. Palatinus, J. Plášil and M. Dušek, *Z. Kristallogr.–Cryst. Mater.*, 2023, **238**, 271–282.
22 A. Saiki, N. Ishizawa, N. Mizutani and M. Kato, *J. Ceram. Assoc. Jpn.*, 1985, **93**, 649–654.
23 A. Z. Khorsand, W. H. Abd Majid, M. E. Abrishami and R. Yousefi, *Solid State Sci.*, 2011, **13**, 251–256.
24 P. Scardi, M. Ermrich, A. Fitch, E. Wen Huang, R. Jardin, R. Kuzel, A. Leineweber, A. Mendoza Cuevas, S. T. Misture, j L. Rebuffik and C. Schimpfg, *J. Appl. Crystallogr.*, 2018, **51**, 831–843.
25 L. Lutterotti, R. Ceccato, R. Dal Maschio and E. Pagani, *Mater. Sci. Forum*, 1998, **278–281**, 87–92.
26 I. C. Madsen, N. V. Y. Scarlett and A. Kern, *Z. Kristallogr.*, 2011, **226**, 944–955.
27 S. Kemethmuller, A. Roosen, F. Goetz-Neunhoeffer and J. Neubauer, *J. Am. Ceram. Soc.*, 2006, **89**, 2632–2637.
28 M. Shepilov, O. Dymshits, I. Alekseeva, A. Hubetsov, D. Shemchuk and A. Zhilin, *J. Non-Cryst. Solids*, 2021, **571**, 121067.
29 S. Tsunekawa, K. Ishikawa, Z.-Q. Li, Y. Kawazoe and A. Kasuya, *Phys. Rev. Lett.*, 2000, **85**, 3440.
30 P. Ayyub, V. R. Palkar, S. Chattopadhyay and M. Multani, *Phys. Rev. B: Condens. Matter Mater. Phys.*, 1995, **51**, 6135–6138.
31 A. Cimino, P. Porta and M. Valigi, *J. Am. Chem. Soc.*, 1966, **49**, 152.
32 G. Li, J. Boerio-Goates, B. F. Woodfield and L. Li, *Appl. Phys. Lett.*, 2004, **85**, 2059.
33 M. C. Spadaro, S. D'Addato, G. Gasperi, F. Benedetti, P. Luches, V. Grillo, G. Bertoni and S. Valeri, *Beilstein J Nanotechnol.*, 2015, **7**, 60–67.
34 Md. Imteyaz Ahmad and S. S. Bhattacharya, *Appl. Phys. Lett.*, 2009, **95**, 191906.
35 V. Swamy, *et al*, *Appl. Phys. Lett.*, 2006, **88**, 233103.
36 D. Prieur, W. Bonani, K. Popa, O. Walter, K. W. Kriegsman, M. H. Engelhard, X. Guo, R. Eloirdi, T. Gouder, A. Beck, T. Vitova, A. C. Scheinost, K. Kvashnina and P. Martin, *Inorg. Chem.*, 2020, **59**, 5760–5767.
37 Y. A. Malinovskii and O. S. Bondareva, *Kristallografiya*, 1991, **36**, 1558–1560.
38 P. M. Diehm, P. Agoston and K. Albe, *Chemphyschem*, 2012, **13**, 2443–2454.
39 S. Deshpande, S. Patil, S. VNT Kuchibhatla and S. Seal, *Appl. Phys. Lett.*, 2005, **87**, 133113.
40 Q. Guo, Y. Zhao, C. Jiang, W. L. Mao, Z. Wang, J. Zhang and Y. Wang, *Inorg. Chem.*, 2007, **46**, 6164–6169.
41 S. BeHgin-Colin, T. Girot, G. Le CaeKr and A. Mocellin, *J. Solid State Chem.*, 2000, **149**, 41–48.
42 T. Atou, K. Kusaba, K. Fukuoka, M. Kikuchi and Y. Syono, *J. Solid State Chem.*, 1990, **89**, 378–384.
43 H. Kishimura, S. Hamada, A. Aruga and H. Matsumoto, *J. Appl. Phys.*, 2016, **119**, 205111.
44 M. Carta, L. Vugrin, G. Miletić, M. J. Kulcsár, P. C. Ricci, I. Halasz and F. Delogu, *Angew. Chem., Int. Ed.*, 2023, **62**, e202308046.

45 S. Mateti, M. Mathesh, Z. Liu, T. Tao, T. Ramireddy, A. M. Glushenkov, W. Yang and Y. I. Chen, *Chem. Commun.*, 2021, **57**, 1080.
46 N. D. Sharma, J. Singh, S. Dogra, D. Varandani, H. K. Poswal, S. M. Sharma and A. K. Bandyopadhyay, *J. Raman Spectrosc.*, 2011, **42**, 438–444.
47 X. Ren, X. Yan, Z. Yu, W. Li, K. Yang, X. Wang, Y. Liu and L. Wang, *Appl. Phys. Lett.*, 2018, **112**, 143102.
48 L. Wang, W. Yang, Y. Ding, Y. Ren, S. Xiao, B. Liu, S. V. Sinogeikin, Y. Meng, D. J. Gosztola, *et al.*, *Phys. Rev. Lett.*, 2010, **105**, 095701.
49 S. Dogra, N. D. Sharma, J. Singh, H. K. Poswal, S. M. Sharma and A. K. Bandyopadhyay, *High Pressure Res.*, 2011, **31**, 292–303.
50 N. S. Lyutsareva, G. A. Berezovskii and I. E. Paukov, *Russ. J. Phys. Chem.*, 1994, **68**, 1064–1067.
51 A. G. De La Torre, S. Bruque and M. A. G. Aranda, *J. Appl. Crystallogr.*, 2001, **34**, 196–202.
52 T. Pickert, M. Balden, M. Rasinski, T. Plocinski, C. Ziebert, F. Koch and H. Maier, *Scr. Mater.*, 2009, **61**, 789–792.
53 K. Chu, Y. Zhang, B. Liu, W. Fang, J. Zhao, W. Li, *et al.*, *J. Am. Ceram. Soc.*, 2025, **108**, e20305.
54 M. Tang, J. A. Valdez, K. E. Sickafus and P. Lu, *Appl. Phys. Lett.*, 2007, **90**, 151907.
55 D. A. Mc Donaill and P. W. M. Jacobs, *J. Solid State Chem.*, 1990, **84**, 183–193.
56 P. D. Battle, C. R. A. Catlow and L. M. Moroney, *J. Solid State Chem.*, 1987, **67**, 42–50.
57 M. Glerup, O. F. Nielsen and F. W. Poulsen, *J. Solid State Chem.*, 2001, **160**, 25–32.
58 V. I. Levitas, *Mater. Trans.*, 2019, **60**, 1294–1301.
59 V. D. Blank and E. I. Estrin, in. *Phase Transitions in Solids under High Pressure*, CRC Press, New York, 2014.
60 F. Delogu, *Scr. Mater.*, 2012, **67**, 340–343.
61 S. S. Aamlid, M. Oudah, J. Rottler and A. M. Hallas, *J. Am. Chem. Soc.*, 2023, **145**, 5991–6006.
62 M. Brahlek, M. Gazda, V. Keppens, A. R. Mazza, S. J. McCormack, A. Mielewczyk-Gryn, B. Musico, K. Page, C. M. Rost, S. B. Sinnott, C. Toher, T. Z. Ward and A. Yamamoto, *APL Mater.*, 2022, **10**, 110902.
63 Y. Gao, X. Tian, Q. Niu and P. Zhang, *ChemSusChem*, 2025, **18**, e202401517.
64 J. Alić, M.-C. Schlegel, F. Emmerling and T. Stolar, *Angew. Chem., Int. Ed.*, 2024, **63**, e202414745.